applied optics

Using a deep neural network for the design of an optical photonic crystal half-subtractor

Pouya Karami,[1] Salah I. Yahya,[2,3] Muhammad Akmal Chaudhary,[4] Maher Assaad,[4] Fariborz Parandin,[1,*] Saeed Roshani,[1] Fawwaz Hazzazi,[5] and Sobhan Roshani[1]

[1]Department of Electrical Engineering, Ker. C., Islamic Azad University, Kermanshah, Iran
[2]Department of Computer Technology Engineering, College of Technical Engineering, Al-Hadba University, Mosul, Iraq
[3]Department of Software Engineering, Faculty of Engineering, Koya University, Koya KOY45, Iraq
[4]Department of Electrical and Computer Engineering, College of Engineering and Information Technology, Ajman University, Ajman 346, United Arab Emirates
[5]Department of Electrical Engineering, College of Engineering, Prince Sattam bin Abdulaziz University, Al-Kharj 11492, Saudi Arabia
*fa.parandin@iau.ac.ir

Received 15 January 2025; revised 9 March 2025; accepted 15 March 2025; posted 17 March 2025; published 4 April 2025

In this paper, a new structure, to our knowledge, for an optical half-subtractor using periodic photonic crystal structures is presented. The difference between this structure and previous ones is that a deep neural network (DNN) is used to optimize the proposed structure. A network composed of silicon rods in air is utilized to achieve the desired structure. The waveguides of this half-subtractor are designed using linear defects and a very small number of point defects. The variable parameters in this simulation are the defect rods, which are optimized by altering them. This structure, due to its simplicity in design and small size, is suitable for use in optical integrated circuits. Another advantage of this structure is the equal power output for the high states. In this study, the plane wave expansion (PWE) method was used to calculate the band structure, and the finite difference time domain (FDTD) method was used to calculate the light emission and output of light power. © 2025 Optica Publishing Group. All rights, including for text and data mining (TDM), Artificial Intelligence (AI) training, and similar technologies, are reserved.

https://doi.org/10.1364/AO.554952

1. INTRODUCTION

The invention of the transistor in the early 1940s was a milestone in the history of electronic technology, leading to significant advancements in the design and performance of electronic circuits [1,2]. This invention enabled the construction of complex circuits and faster, more reliable processors. Since the invention of the transistor, there have been many advancements in electronic technology, including the reduction in transistor dimensions, the increase in the number of transistors in an integrated circuit, and improvements in processor efficiency and speed [3,4]. However, with the advancement in technology and the reduction in transistor dimensions, numerous problems have also arisen. The reduction in transistor dimensions has led to issues such as a significant increase in power consumption and heat emission. These problems, due to the increased transistor density and thermal interference, reduce the efficiency and lifespan of devices [5–7]. Additionally, as dimensions shrink, quantum effects such as electron tunneling become a serious issue, causing disruptions in transistor performance and signal instability. Furthermore, design and manufacturing complexities have added to the difficulties associated with reducing processor size [8,9].

In this context, optical processing has garnered considerable attention as an attractive alternative due to its capabilities in offering much higher processing speeds compared to electronic processing at similar scales [7,10]. The use of photonic crystals, as a novel technology, can help overcome current limitations in digital processing and enhance the performance of electronic systems [11]. Photonic crystals, composed of a combination of two or more materials with different refractive indices, are structures with unique optical properties capable of controlling and guiding light in specific paths [12]. These structures are generally classified into three categories: one-dimensional, two-dimensional, and three-dimensional [13]. One-dimensional photonic crystals, which are periodic in one dimension, are typically used in simpler applications for creating filters and waveguides. Two-dimensional photonic crystals, which are periodic in two dimensions, offer more features than the one-dimensional type and are widely used in designing various optical circuits and sensors [14]. These structures are popular due to their simplicity in design and ability to control light in two dimensions. Three-dimensional photonic crystals, periodic in all three dimensions, possess unique characteristics due to their ability to reflect light in three different directions, making them highly suitable for use in optical devices [15]. These

structures can effectively guide and control light in complex spaces and, as a result, are used in designing advanced optical devices. However, the construction of these crystals is limited due to high technical complexities and costs, and thus, two-dimensional photonic crystals are often used instead of three-dimensional ones in many applications [16].

Due to their unique properties in guiding and controlling light, photonic crystals have numerous applications in optical electronics. These structures are effective in designing optical circuits, filters, waveguides, and optical sensors and can improve the performance of optical fibers [17]. Additionally, photonic crystals are used to create optical logic gates, half-subtractors, half-adders, and special optical devices such as lasers [18–20].

Numerous efforts have been made to develop optical devices utilizing photonic crystals [21,22]. Some research studies have explored the design of various digital logic gates using photonic crystal technology [23,24]. In some cases, a single structure has been adapted to function as different logic gates by altering the inputs. However, there has been limited research on the design of more complex logic circuits, such as half-adders and half-subtractors, based on photonic crystals.

Also, neural networks and deep learning can be used as new tools to help design optical devices with better performance [25–27]. For instance, deep learning approaches have been successfully employed in [28,29] to reduce the dimensionality of complex optical design problems while maintaining high accuracy. Similar methodologies have revealed fundamental insights into light–matter interactions and enabled the design of reconfigurable optical devices [30,31]. In addition to ANN-driven optimizations, other advanced design methodologies, such as cascaded metasurface optimization [32] and nonlinear geometric phase coding in soft-matter photonics [33], demonstrate the broader trend toward employing complex computational techniques to enhance optical device performance.

Half-subtractors, as one of the essential components in optical processing, have many applications, including designing and constructing complex optical devices, optical communication systems, and optical signal processing. These components can play a significant role in filtering and dividing optical signals, improving the efficiency of imaging systems, and increasing accuracy in optical measurements. The ability to appropriately distinguish between logical states "0" and "1" in the half-subtractor reduces errors in output detection and therefore has a significant impact on the performance and accuracy of optical integrated circuits. This research can be considered an important step toward the improvement and development of optical processors and digital circuits with high speed and accuracy, demonstrating the high potential of photonic crystals in designing and constructing advanced optical circuits.

In [34], an optical subtractor utilizing a photonic crystal structure is presented. This structure incorporates silicon rods with a circular cross-section embedded in an air platform and is optimized based on photonic band gap principles. In this structure, a ring resonator is used, which can lead to an oversized structure. An all-optical subtractor is presented in [35] based on two-dimensional photonic crystals. The results of this work have shown that the defect rods can be used in a half-subtractor structure to improve the performance.

In this paper, the main goal was to design and develop an optical half-subtractor based on two-dimensional photonic crystals. The use of this proposed structure is particularly important in constructing optical integrated circuits. The designed logical gate characteristics result is improved using the deep neural network.

2. PROPOSED ALL-OPTICAL HALF-SUBTRACTOR

A half-subtractor is a circuit that performs the subtraction of two single-bit numbers. In this circuit, two bits, X and Y, are considered as inputs, and two outputs, Difference (D) and Borrow (B), are generated. Table 1 shows the truth table of a half-subtractor. The design of the proposed half-subtractor is based on Table 1.

In the proposed structure for creating the optical half-subtractor, a two-dimensional photonic crystal structure with a cubic lattice is used, consisting of silicon rods in an air substrate. The physical characteristics of the structure, including the rod radius, lattice constant, refractive index of the rods, and other parameters, are precisely provided in Table 2.

The photonic band gap (PBG) of the structure is in the TM mode, with a range specified between 1.42 and 2.14 μm, as shown in Fig. 1. This forbidden band range is analyzed using the normalized parameter a/λ, making the results generalizable and comparable, and is expressed as $0.28 < a/\lambda < 0.42$. As a result, wavelengths shorter than 1.42 μm and longer than 2.14 μm pass through the structure, while wavelengths between these two values do not. Considering these characteristics, the wavelength of the input sources is selected to be 1.55 μm, a commonly used wavelength in optical communications.

The simulation results for the refractive index of the structure are shown in Fig. 2. As indicated in the figure, the background refractive index is one, and the refractive index of the rods is 3.46.

To realize the all-optical half-subtractor, as shown in Fig. 3, by removing several rods from the left side, two paths for the waveguides and light propagation from the X and Y input sources are created. Two waveguide paths for the Difference (D) and Borrow (B) outputs are formed by removing additional rods.

Table 1. Truth Table of the Logical Half-Subtractor

X	Y	B	D
0	0	0	0
0	1	1	1
1	0	0	1
1	1	0	0

Table 2. Parameters of the Initially Proposed Photonic Crystal Structure

Parameters	Symbol	Value
Lattice constant	a	0.6 μm
Radius of rods	R	0.12 μm
Background refractive index	n1	1
Rods refractive index	n2	3.46
Number of rods	–	21 × 15

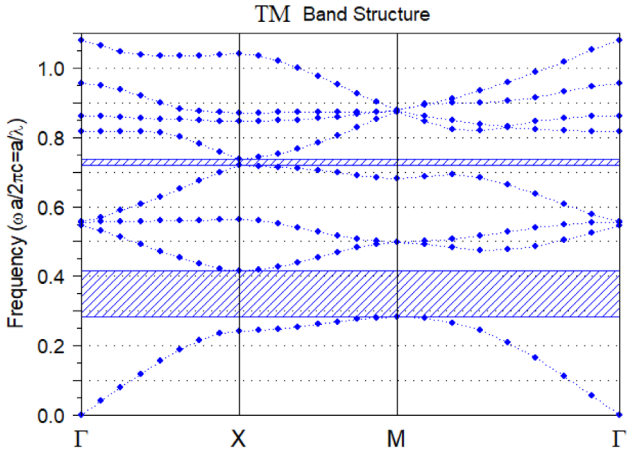

Fig. 1. Normalized photonic band gap diagram in TM Mode.

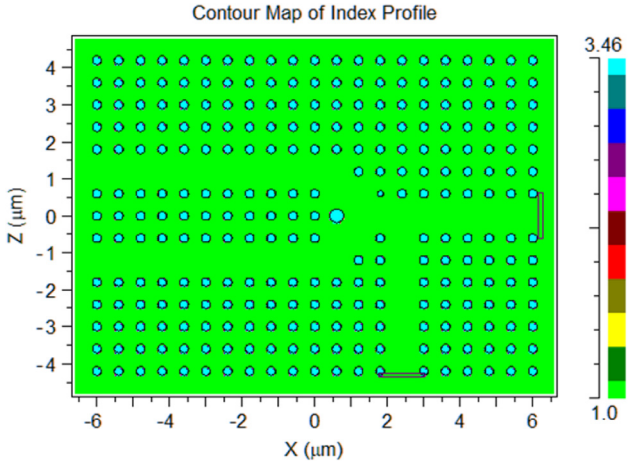

Fig. 2. Refractive index diagram of the structure.

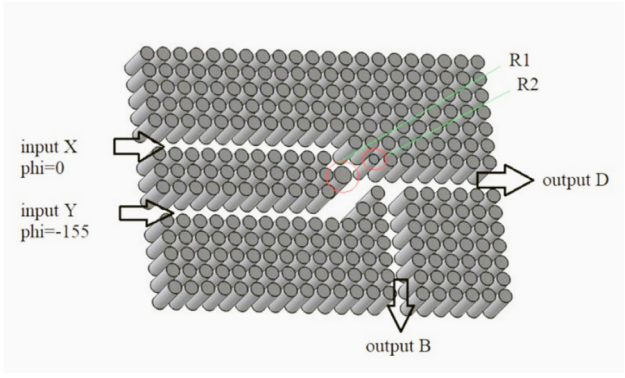

Fig. 3. Initially proposed structure for the all-optical half-subtractor.

Two defect rods, R1 and R2, and a phase shift of −155 deg for the Y source have been utilized to achieve better initial results.

Since light propagation in photonic crystal waveguides is based on the interaction of light and matter, the radius of the rods in the waveguide paths affects the light propagation from the waveguides. This property has been used to create a logical half-subtractor and propagate light to the outputs in different modes.

3. ANN MODELING OF THE HALF-SUBTRACTOR STRUCTURE

In this section, we employed an artificial neural network (ANN) to optimize the dimensions of the defect rods (R1 and R2) and the phase difference of the input laser sources in the proposed photonic crystal half-subtractor structure. The neural network was trained to refine these parameters in order to enhance the accuracy and efficiency of the optical subtraction operation. The neural network used in this study is a feedforward neural network with a multi-layer perceptron (MLP) structure, which is particularly suitable for function approximation tasks. The network architecture was configured with three hidden layers, each containing seven neurons, and this structure is repeated for each output, as shown in Fig. 4.

In order to identify the optimal neural network architecture for modeling the proposed half-subtractor, we tested multiple configurations with different numbers of hidden layers and neurons. Each configuration is evaluated using the mean squared error (MSE) metric on training data, as shown in Fig. 5. It can be seen that networks with three hidden layers are more accurate than networks with two hidden layers. Among all tested configurations, the network with three hidden layers and seven neurons in each layer achieved the lowest MSE, indicating superior performance and convergence. Therefore, this architecture is selected to model the proposed half-subtractor.

The activation functions used in the hidden layers were "tansig" (hyperbolic tangent sigmoid), which is well-suited for handling nonlinear relationships between inputs and outputs, and a "linear" activation function was used in the output layer. The input to the neural network consisted of the extracted values for the defect rods R1 and R2, as well as the phase difference of the input lasers. These inputs were crucial as they directly influence the photonic band gap and the optical path within the structure, thereby affecting the logic states of the half-subtractor.

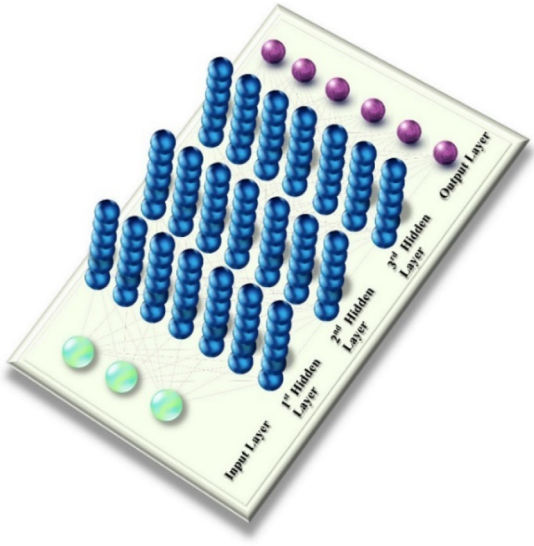

Fig. 4. Architecture of the proposed ANN to model the designed all-optical half-subtractor structure.

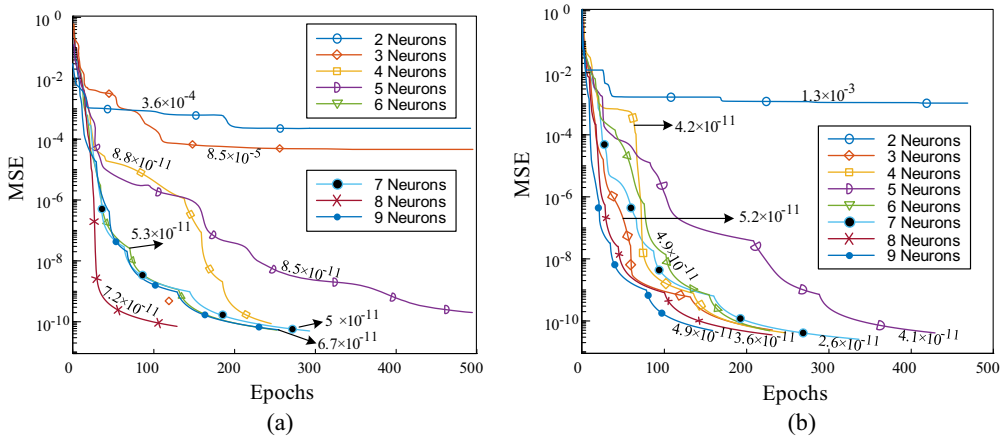

Fig. 5. Mean squared error (MSE) comparisons for different neural network configurations. (a) MSE plots for networks with two hidden layers and different numbers of neurons. (b) MSE plots for networks with three hidden layers and different numbers of neurons.

The outputs of the neural network corresponded to the four logical states of the half-subtractor gate, allowing the network to learn and predict the optimal settings that would yield the desired output for each state.

The predicted output of the proposed neural network can be defined as written in Eq. (1):

$$\hat{Y} = f(W_3 \times \text{tansig}(W_2 \times \text{tansig}(W_1 \times X + B_1) + B_2) + B_3). \tag{1}$$

In Eq. (1), W_i are the weights, and B_i are the biases between the neurons in different layers. Also, "tansig" is the hyperbolic tangent sigmoid activation function between hidden layers, and X is the input vectors, which are considered defect rod dimensions and phase shifts in the proposed model. The hyperbolic tangent sigmoid activation function is written in Eq. (2):

$$\text{tansig}(Z) = \frac{2}{1 + e^{-2Z}} - 1. \tag{2}$$

By substituting the hyperbolic tangent sigmoid activation function in Eq. (1) and considering the linear activation function for the output layer, the final predicted outputs can be written in Eq. (3):

$$\hat{Y} = W_3 \times \left(\frac{2}{1 + e^{-2\left(W_2 \times \left(\frac{2}{1+e^{-2(W_1 \times X + B_1)}} - 1\right) + B_2\right)}} - 1 \right) + B_3. \tag{3}$$

The training results of the proposed ANN model are depicted in Fig. 6. According to the obtained results in the training phase, the network is trained with high precision and very low errors. The gradient values represent the sensitivity of the loss function, indicating how much it would change with slight adjustments to the network weights. A declining gradient suggests that the model is converging. When the gradient becomes extremely small, it signals that the network has likely reached a local minimum. Additionally, the μ values correspond to the learning rate parameter used in the Levenberg–Marquardt (LM) optimization algorithm during training.

The results of the test and train procedures of the proposed ANN model are illustrated in Fig. 7. As seen, the proposed model has succeeded in recognizing the hidden relation between the input and output parameters of the all-optical half-subtractor logical gates in both training and testing phases. The ANN was trained using a backpropagation feedforward algorithm, with the dataset divided into training and testing subsets. The training process focused on minimizing the MSE.

Table 3 presents the error metrics for the proposed ANN model during both the training and testing phases across different logical states. The table highlights the mean absolute error (MAE) and MSE values, demonstrating that the model performs exceptionally well during training, with error values being close to zero. However, the testing phase shows higher error values, particularly for the MAE, indicating that the model encounters more difficulty when predicting unseen data.

4. RESULTS

Based on the results obtained from the neural network method, the values of R1 = 1.6R, R2 = 0.7R, and phase = −155 deg have been considered suitable values in this design. The analysis of the photonic band structure was performed using the plane wave expansion (PWE) method, and the light propagation analysis within the structure was conducted using the finite difference time domain (FDTD) method. RSoft software was used to apply these methods. By utilizing the FDTD method, the optical characteristics of the structure, including its response to different wavelengths and the performance of the half-subtractor, can be evaluated. The proposed structure was then simulated and analyzed for four different states.

The solution of Maxwell's equations was used by the FDTD method to calculate the optical power at the output and how the light propagates in the waveguide paths. Maxwell's equations include four basic equations that can be used to analyze the behavior of light in an environment. These equations in the photonic crystal environment are shown in Eqs. (4)–(6) due to the absence of electric charge [8]:

$$\nabla \times \boldsymbol{E}(\boldsymbol{r}, \boldsymbol{t}) = -\frac{\partial \boldsymbol{B}}{\partial t}, \quad \nabla . \boldsymbol{B} = 0, \tag{4}$$

$$\nabla \times \boldsymbol{H} = \frac{\partial \boldsymbol{D}}{\partial t}, \quad \nabla . \boldsymbol{D} = 0, \tag{5}$$

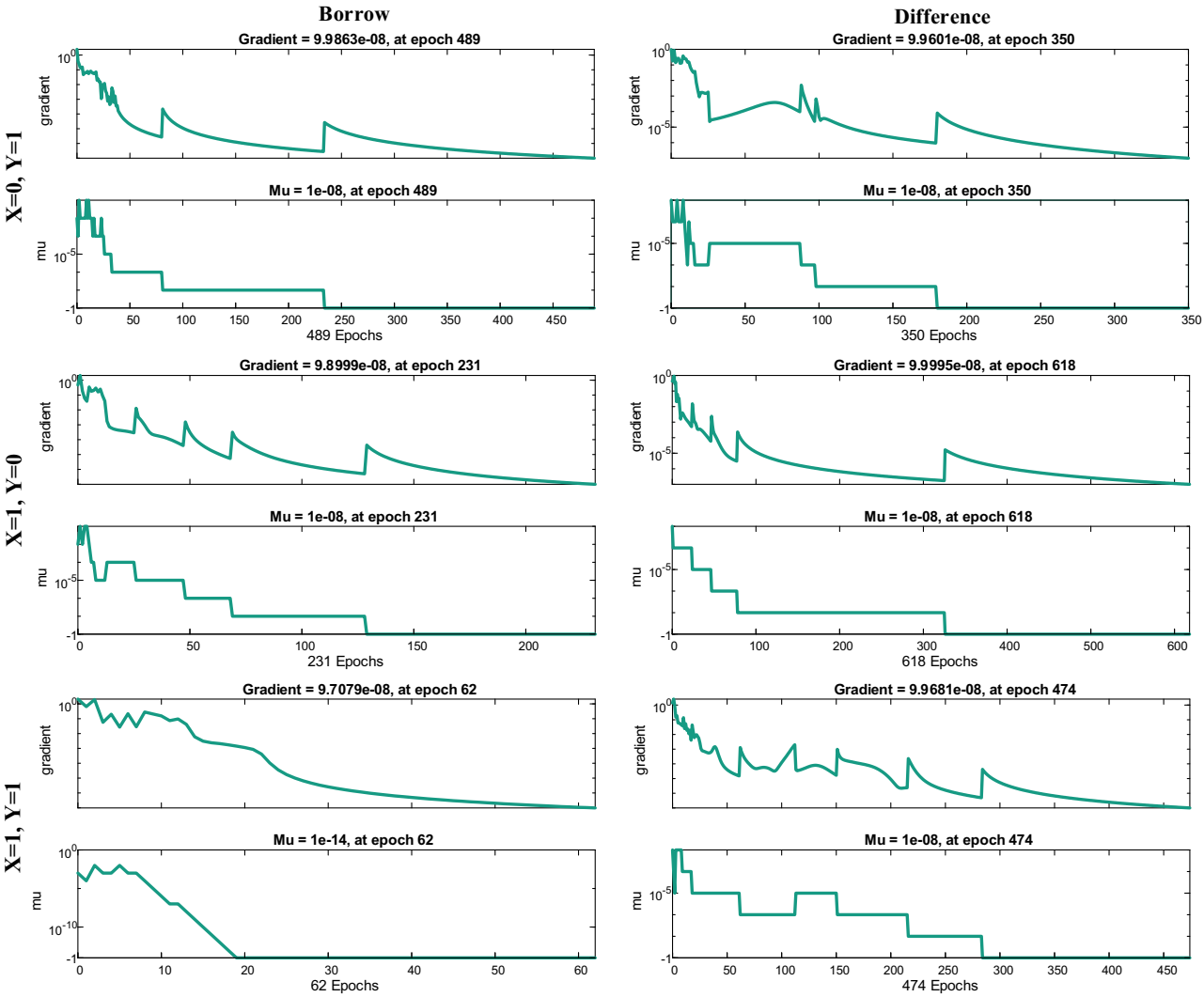

Fig. 6. Training results of the proposed ANN model.

$$\boldsymbol{D} = \varepsilon_0 \varepsilon_r \boldsymbol{E}, \quad \boldsymbol{B} = \mu_0 \mu_r \boldsymbol{H}, \tag{6}$$

where **E** and **H** are the electric and magnetic fields in these relationships, respectively, and **B** and **D** are the magnetic and displacement induction fields, respectively. For most dielectric materials of interest, the relative magnetic permeability is close to unity, and it can be set to $\boldsymbol{B}(\boldsymbol{r}, t) = \mu_0 \boldsymbol{H}(\boldsymbol{r}, t)$. In the above relations, ε_0 and ε_r are the permittivity vacuum and relative permittivity, respectively. Also, μ_0 is the vacuum permeability.

The answers $E(r, t) = E(r)e^{-i\omega t}$ and $H(r, t) = H(r)e^{-i\omega t}$ are assumed to solve Maxwell's equations. For the photonic band, the gaps are wider for the electric field in photonic crystals. Thus, TE modes are calculated. Finally, by the combination of the proposed answers and the original Maxwell's equations, the equation for TM polarization can be obtained as [8]

$$\nabla \times \left(\frac{1}{\varepsilon(\boldsymbol{r})} \nabla \times \boldsymbol{H}(\boldsymbol{r}) \right) = \left(\frac{\omega}{c} \right)^2 \boldsymbol{H}(\boldsymbol{r}). \tag{7}$$

In the first logical state (X = 0, Y = 0), both sources are off, resulting in no power passing through either output, and the power at both outputs is zero. In the second logical state (X = 0, Y = 1), only the Y source is on. The power enters the structure through the waveguide path associated with Y, and due to the presence of defect rods R1 and R2, half of the power exits through the D output, and the other half exits through the B output. Figure 8(a) shows the power distribution diagram within the structure, and Fig. 8(b) shows the normalized power at the outputs.

In the third logical state (X = 1, Y = 0), the X source is on, and the Y source is off. The output power from the X source enters the structure through the corresponding waveguide path, and due to the defect rods, the power from this source only passes through the waveguide leading to the D output. Figure 9(a) shows the distributed power in the waveguides and outputs, and Fig. 9(b) displays the normalized power at the outputs.

In the fourth logical state (X = 1, Y = 1), both X and Y sources are on. The power from the sources enters the structure through the X and Y waveguide paths, and due to the −155 deg phase difference of the Y source wave relative to the X source, almost all the power is dissipated within the structure. This dissipation occurs because the phase difference causes the two

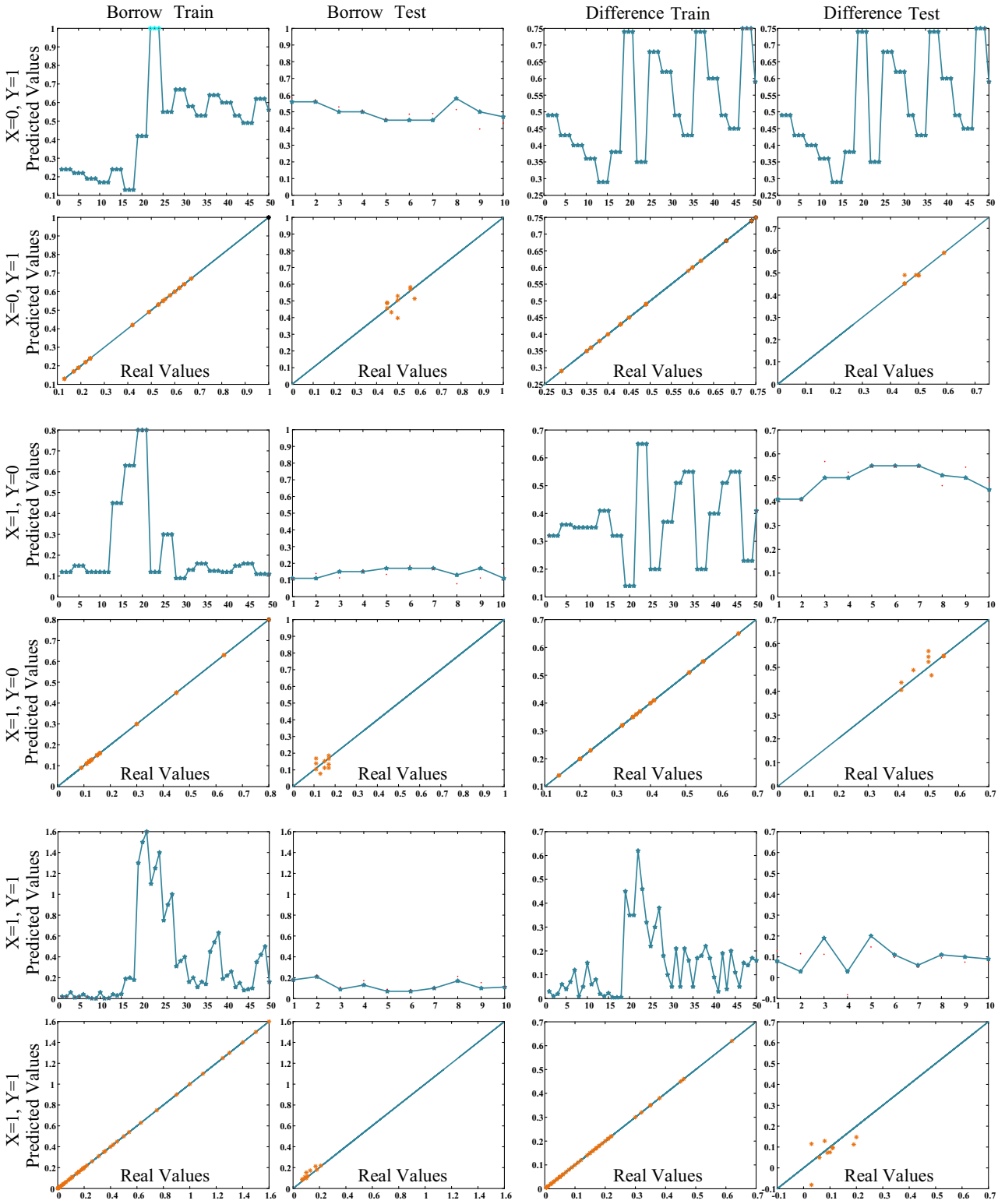

Fig. 7. Performance analysis of the proposed ANN model. Each row and column of figures represents the logical states and the corresponding Borrow or Difference output. The first to fourth columns of subfigures are related to Borrow train, Borrow test, Difference train, and Difference test results. Also, the first two rows of subfigures show the model results for the logical state $X = 0, Y = 1$; the second two rows are related to the logical state $X = 1, Y = 0$; and the third two rows are corresponding to the logical state $X = 1, Y = 1$.

identical waves to cancel each other out. Therefore, only a very small amount of power passes through the D and B outputs, which can be considered the logical zero state. Figure 10(a) shows the distributed power in the waveguides and outputs, and Fig. 10(b) displays the normalized power at the outputs. Table 4 summarizes the output values in the different input states.

Table 3. Error Results of the Proposed ANN Model during the Training and Testing Phases

Logical State	MAE (Train)	MAE (Test)	MSE (Train)	MSE (Test)
A = 0, B = 1 (Borrow)	1.1191e−06	0.0356	2.0720e−11	0.0021
A = 0, B = 1 (Difference)	2.8752e−06	0.0078	1.6182e−11	1.9651e−04
A = 1, B = 0 (Borrow)	1.1349e−06	0.0300	2.6158e−11	0.0013
A = 1, B = 0 (Difference)	4.3023e−07	0.0256	3.1177e−12	0.0011
A = 1, B = 1 (Borrow)	4.3029e−08	0.0210	4.1312e−15	7.5239e−04
A = 1, B = 1 (Difference)	5.6968e−07	0.0455	1.5466e−11	0.0032

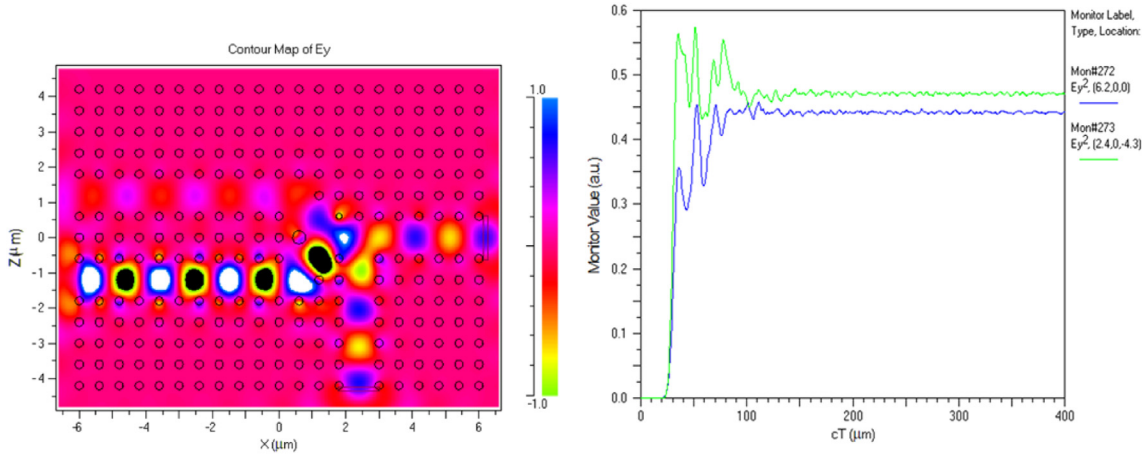

Fig. 8. Outputs in the state X = 0, Y = 1: (a) power distribution in the waveguides and (b) normalized power diagram at the outputs.

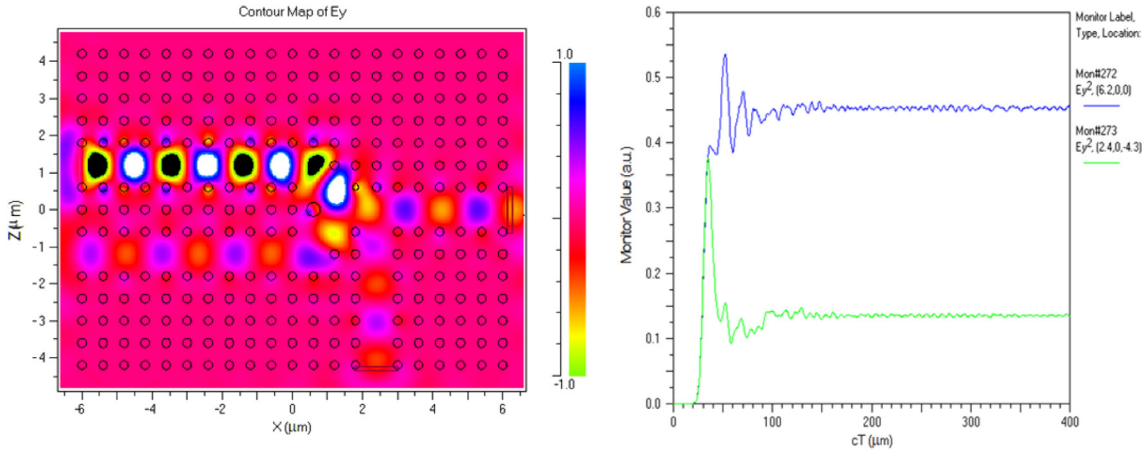

Fig. 9. Outputs in the state X = 1, Y = 0: (a) power distribution in the waveguides and (b) normalized power diagram at the outputs.

The results obtained from Table 3 indicate that the designed structure can be used as a half-subtractor because it matches the truth table accurately. The advantages of this design include the simplicity of the structure and the use of minimal defect rods. The small size of the structure is also an advantage. The time for the output to reach a stable state is very short, so it can be concluded that this structure has a low delay time, making it suitable for use in high-speed circuits.

A comparison between the performance of the proposed design and related works is listed in Table 5. The proposed design is of a small size, making it suitable for use in integrated circuits. The structure in [36], as shown in the table, has much larger dimensions compared to the proposed gate, which prevents its use in optical integrated circuits. In the structures presented in [36,37], a very important design consideration has been overlooked, which is that the input and output locations are placed next to each other. This design flaw makes it difficult to use these structures in optical integrated circuits. Other advantages of the proposed all-optical gate are the low energy consumption and the minimal number of sources required. In contrast, the structure in [36] uses several additional sources, and in the structures proposed in [35–37], the energy consumption of their sources is 1.5 to 2 times that of the structure in the proposed work.

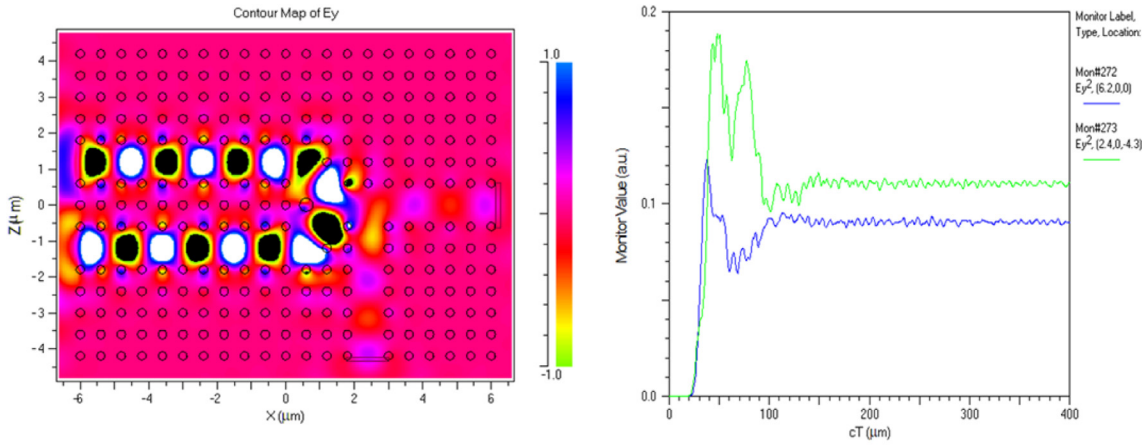

(a) (b)

Fig. 10. Outputs in the state X = 1, Y = 1: (a) power distribution in the waveguides and (b) normalized power diagram at the outputs.

Table 4. Output Power in Different Input States

Input		Output	
		Borrow	Difference
X	Y	(Normalized Power)	(Normalized Power)
0	0	0	0
0	1	0.47	0.45
1	0	0.11	0.45
1	1	0.11	0.49

5. CONCLUSION

In this study, a low-dimensional photonic crystal structure was used to design an optical half- subtractor. Optical power was used to stimulate the inputs. High and low logic was based on the optical power levels of the light sources. The PWE and FDTD methods were used in the analysis of this structure. The presented deep neural network model was used to improve the performances of the proposed gate. The results show that the proposed structure has appropriate powers in both high and low logic states. The simplicity of the structure, the use of fewer rods, and the minimal number of defect rods make this structure suitable for designing integrated optical circuits.

Disclosures. The authors declare no conflicts of interest.

Data availability. All data will be provided by the authors upon request.

REFERENCES

1. Q. Li, Y. Yang, Y. Wen, *et al.*, "A fast overcurrent protection IC for SiC MOSFET based on current detection," IEEE Trans. Power Electron. **39**, 4986–4990 (2024).
2. Q. Li, Y. Yang, Y. Wen, *et al.*, "Active gate driver with the independent suppression of overshoot and oscillation for SiC MOSFET modules," IEEE Trans. Indus Electron. **72**, 2325–2335 (2024).
3. H. Yuan, Y. Huang, T. Gong, *et al.*, "Spatial and energetic mapping of traps in FeFET during endurance process by advanced trap characterization platform," IEEE Electron Dev. Lett. **45**, 2371–2374 (2024).
4. D. X. Chen, Y. Wang, Y. X. Song, *et al.*, "TCAD analysis of single-event burnout Hardness for an improved CoolSiC trench MOSFET," IEEE Trans. Electron Dev. **71**, 4596–4603 (2024).
5. H. S. P. Wong and S. Salahuddin, "Memory leads the way to better computing," Nat. Nanotechnol. **10**, 191–194 (2015).
6. K. Bernstein, R. K. Cavin, W. Porod, *et al.*, "Device and architecture outlook for beyond CMOS switches," Proc. IEEE **98**, 2169–2184 (2010).
7. N. Mohammadi, G. Moloudian, S. Roshani, *et al.*, "A Wilkinson power divider with harmonic suppression through low-pass filter for GSM and LTE applications," Sci. Rep. **14**, 2429 (2024).
8. J. D. Joannopoulos, S. G. Johnson, J. N. Winn, *et al.*, *Photonic Crystal: Molding the Flow of Light* (Princeton University, 1995).
9. S. John, "Strong localization of photons in certain disordered dielectric superlattices," Phys. Rev. Lett. **58**, 2486 (1987).
10. S. Roshani, S. Koziel, S. I. Yahya, *et al.*, "Mutual coupling reduction in antenna arrays using artificial intelligence approach and inverse neural network surrogates," Sensors **23**, 7089 (2023).
11. K. N. Sediq, F. F. Muhammadsharif, S. O. Ramadan, *et al.*, "Design and study of a nanocavity-based one-dimensional photonic crystal for potential applications in refractive index sensing," Aro-Sci. J. Koya Univ. **11**, 95–98 (2023).
12. K. Sakoda and K. Sakoda, *Optical Properties of Photonic Crystals* (Springer, 2005).

Table 5. Comparison between Performance of the Proposed Design and Related Works

Reference	Borrow A = B = 0	Difference A = B = 0	Borrow A = 0, B = 1	Difference A = 0, B = 1	Borrow A = 1, B = 0	Difference A = 1, B = 0	Borrow A = B = 1	Difference A = B = 1	Size (μm²)	Integration Ability	Delay Time (Ps)	Lasers Power
This work	0%	0%	47%	45%	11%	45%	11%	9%	96	Yes	0.09	100%
[35]	0%	0%	44%	53%	10%	55%	11%	6%	132	Yes	0.1	150%
[36]	0%	0%	85%	90%	5%	78%	12%	6%	672	No	0.4	200%
[37]	0%	0%	46%	53%	9.5%	53%	9.5%	8%	108	No	0.1	200%

13. S. Noda, K. Tomoda, N. Yamamoto, *et al.*, "Full three-dimensional photonic bandgap crystals at near-infrared wavelengths," Science **289**, 604–606 (2000).
14. K. Inoue and K. Ohtaka, *Photonic Crystals: Physics, Fabrication and Applications* (Springer, 2004).
15. Q. Xu, B. Schmidt, S. Pradhan, *et al.*, "Micrometre-scale silicon electro-optic modulator," Nature **435**, 325–327 (2005).
16. B. R. Singh and S. Rawal, "Photonic-crystal-based all-optical NOT logic gate," J. Opt. Soc. Am. A **32**, 2260–2263 (2015).
17. T. Baba, "Slow light in photonic crystals," Nat. Photonics **2**, 465–473 (2008).
18. G. E. Hinton, S. Osindero, and Y. W. Teh, "A fast learning algorithm for deep belief nets," Neural Comput. **18**, 1527–1554 (2006).
19. P. Karami, S. I. Yahya, M. K. Chaudhary, *et al.*, "Design of a photonic crystal exclusive-OR gate using recurrent neural networks," Symmetry **16**, 820 (2024).
20. F. Parandin, P. Karami, and A. Mohammadi, "Machine learning-driven optimization of photonic crystal structures for superior optical NOR gate performance," Dimensions **14**, 16 (2024).
21. M. A. Butt and S. N. Khonina, "Recent advances in photonic crystal and optical devices," Crystal **14**, 543 (2024).
22. D. G. Sankar Rao, M. S. Fathima, P. Manjula, *et al.*, "Design and optimization of all-optical demultiplexer using photonic crystals for optical computing applications," J. Opt. Commun. **44**, s197–s202 (2024).
23. T. F. Krauss and M. Richard, "Photonic crystals in the optical regime—past, present and future," Prog. Quantum Electron. **23**, 51–96 (1999).
24. M. Notomi, "Theory of light propagation in strongly modulated photonic crystals: refractionlike behavior in the vicinity of the photonic band gap," Phys. Rev. B **62**, 10696 (2000).
25. S. B. Neamah and A. A. Karim, "Real-time traffic monitoring system based on deep learning and YOLOv8," Aro-Sci. J. Koya Univ. **11**, 137–150 (2023).
26. B. Wang, W. Chen, J. Qian, *et al.*, "Single-shot super-resolved fringe projection profilometry (SSSR-FPP): 100,000 frames-per-second 3D imaging with deep learning," Light Sci. Appl. **14**, 70 (2025).
27. Y. Wang, Y. Wang, A. Yu, *et al.*, "Non-interleaved shared-aperture full-stokes metalens via prior-knowledge-driven inverse design," Adv. Mater. **10**, 2408978 (2024).
28. Y. Kiarashinejad, S. Abdollahramezani, and A. Adibi, "Deep learning approach based on dimensionality reduction for designing electromagnetic nanostructures," NPJ Comput. Mater. **6**, 12 (2020).
29. Y. Kiarashinejad, M. Zandehshahvar, S. Abdollahramezani, *et al.*, "Knowledge discovery in nanophotonics using geometric deep learning," Adv. Intell. Syst. **2**, 1900132 (2020).
30. O. Hemmatyar, S. Abdollahramezani, Y. Kiarashinejad, *et al.*, "Full color generation with fano-type resonant hfo 2 nanopillars designed by a deep-learning approach," Nanoscale **11**, 21266–21274 (2019).
31. Y. Kiarashinejad, S. Abdollahramezani, M. Zandehshahvar, *et al.*, "Deep learning reveals underlying physics of light–matter interactions in nanophotonic devices," Adv. Theor. Simul. **2**, 1900088 (2019).
32. X. Li, X. Cai, C. Liu, *et al.*, "Cascaded metasurfaces enabling adaptive aberration corrections for focus scanning," Opto-Electron. Adv. **7**, 240085 (2024).
33. J. T. Pan, B. H. Zhu, L. L. Ma, *et al.*, "Nonlinear geometric phase coded ferroelectric nematic fluids for nonlinear soft-matter photonics," Nat. Commun. **15**, 8732 (2024).
34. F. Parandin and A. Sheykhian, "Designing a circuit for high-speed optical logic half subtractor," Int. J. Circuits Syst. Signal Process. **16**, 887–891 (2022).
35. F. Parandin, M. R. Malmir, and M. Naseri, "All-optical half-subtractor with low-time delay based on two-dimensional photonic crystals," Superlattices Microstruct. **109**, 437–441 (2017).
36. A. Askarian, G. Akbarizadeh, and M. Fartash, "A novel proposal for all optical half-subtractor based on photonic crystals," Opt. Quantum Electron. **51**, 1–9 (2019).
37. F. Parandin, R. Kamarian, and M. Jomour, "A novel design of all optical half-subtractor using a square lattice photonic crystals," Opt. Quantum Electron. **53**, 114 (2021).